

**Effect of cathode on crosstalk in Si-based lithium-ion cells**

Journal:	<i>Journal of Materials Chemistry A</i>
Manuscript ID	TA-ART-07-2021-006304.R3
Article Type:	Paper
Date Submitted by the Author:	16-Nov-2021
Complete List of Authors:	Kim, Minkyu; Argonne National Laboratory, Yang, Zhenzhen; Argonne National Laboratory, Chemical Science and Engineering Son, Seoung-Bum ; Argonne National Laboratory Trask, Stephen; Argonne National Laboratory, Chemical Sciences and Engineering - Electrochemical Energy Storage Jansen, Andrew; Argonne National Laboratory, Chemical Sciences and Engineering Division Bloom, Ira; Chemical Sciences and Engineering Division, Argonne National Laboratory

Effect of cathode on crosstalk in Si-based lithium-ion cells

Minkyu Kim, Zhenzhen Yang*, Seoung-Bum Son, Stephen E. Trask, Andrew Jansen, Ira Bloom*

Chemical Science and Engineering Division, Argonne National Laboratory, 9700 South Cass Avenue, Lemont, IL 60439, USA

* Corresponding author: yangzhzh@anl.gov, ira.bloom@anl.gov

Abstract

Crosstalk between the cathode and the anode in Li-ion batteries has a great impact on performance, safety and cycle lifetime. However, a systematic investigation of crosstalk behavior in silicon (Si)-based cells with various cathode materials has not been reported. We investigated the crosstalk behavior of a Si anode coupled with one of the following cathodes—LiCoO₂ (LCO), LiNi_{0.5}Mn_{0.3}Co_{0.2} (NMC532), and LiFePO₄ (LFP)—in a full cell. For each electrochemical couple, we compared electrolyte decomposition products, solid electrolyte interphase (SEI) chemistry, and degradation mechanisms during cycling. From a very early stage of cycling, each couple showed different crosstalk behavior; different electrolyte decomposition products and SEI chemistry on the Si anodes were seen. Specifically, the formation and growth mechanism of Si SEI differ depending on cathode materials. For the LFP system, the Si SEI rich in LiF and inorganic species, which is stable and robust. It forms at an early stage of cycle. As a result, the SEI of Si from the LFP system well tolerates SEI breakage due to mechanical changes of Si and suppresses Li loss, resulting in stable cycle life.

1. Introduction

Lithium-ion batteries (LIBs) have been widely used as power sources for various portable devices. Recently, their use has been extended to larger applications, such as electric vehicles (EVs).¹ As the demand for pure EVs with longer driving range increases, LIBs with high gravimetric/volumetric energy density become necessary. Therefore, many efforts have been devoted to the development of new energy-dense electrode materials.¹⁻²

Silicon (Si) is being explored to answer the demand for a high-energy-density battery, since it has a very high gravimetric/volumetric energy density of 3579 mAh/g or 2194 Ah/L (to $\text{Li}_{15}\text{Si}_4$).³ Therefore, Si-based anodes have a greater potential to meet the energy demands for transportation applications than the conventional graphite anode (cf. 372 mAh/g or 719 Ah/L to LiC_6).⁴ However, the Si anode faces many critical challenges in reaching a long cycle life.⁴⁻⁶ So understanding the degradation mechanism of the Si anode is very important for fully exploiting its potential.

Recently, crosstalk between cathode and anode in full cells has been increasingly recognized as an issue in LIBs because it has a significant impact on performance, safety and cycle life.⁷⁻¹⁸ In the broadest sense, crosstalk can be defined as chemical or electrochemical side reactions at one electrode that affect the properties of the other electrode. One of the most widely observed manifestations of crosstalk is transition metal dissolution and migration. Transition metal ions in the cathode, such as Ni, Co or Mn, can dissolve, migrate and deposit on the graphite anode during the cycling of a LIB.^{7-8, 13-14, 19} Though there are debates on the exact mechanism of transition metal dissolution, it is widely understood that transition metal dissolution can lead to rapid Li loss and/or changes in the solid electrolyte interphase (SEI) layer chemistry on the anode.^{10, 12-13} Crosstalk can also affect the electrolyte decomposition mechanism. Sahore et al.¹⁸ recently identified some crosstalk species, which are generated at one electrode, diffuse to the other, and react there. These species likely contain C=C or C-F bonds, which have rarely been observed in electrolyte decomposition species.¹⁸ Since the degradation of a Si anode is highly dependent on the properties of the SEI layer,²⁰⁻²⁴ understanding the crosstalk phenomenon in Si-based LIBs is very important. However, systematic investigations of crosstalk and its effect on performance of the full cell have not been widely reported.

Here, for the first time, we systematically investigated crosstalk and its effect on Si anode properties, such as electrochemistry and SEI chemistry, in Si-based full cells with various cathode

materials. For this purpose, we paired Si-based anodes with one of the following cathode materials: LiCoO₂ (LCO system), LiNi_{0.5}Mn_{0.3}Co_{0.2} (NMC532 system), or LiFePO₄ (LFP system). Each full-cell system was aged for 50 cycles, and the electrochemistry of each cell system was then compared. Post-test analysis was performed in each system after 2 cycles and after 50 cycles of cycle life test. The aged electrolyte was analyzed by high-performance liquid chromatography coupled with electrospray ionization mass spectroscopy (HPLC/ESI-MS). The SEI chemistry on each harvested Si anode was characterized by X-ray photoelectron spectroscopy (XPS). The harvested cathodes and anodes from these systems were re-assembled in half cells, and the resulting electrochemical behavior was compared to understand how crosstalk affected the degradation of each electrode material.

2. Results and Discussion

2.1. Si anode degradation

Since Si anode degradation is highly dependent on the lower cutoff potential²⁴, it is very important to compare the electrochemical performance with the same lower cutoff potential of Si coupled with each cathode system. We set the upper cutoff potential at 4.1V for LCO & NMC532 systems, and at 3.7V for LFP system. We confirmed that in the three-electrode cells the initial cycle of lower cutoff potential of Si anode was set at ~0.1V: 0.107V for Si in LCO system, 0.103V for Si in NMC532 system, 0.099V in LFP system (Fig. S1). Fig. 1a shows cycle life performance of the three different types of full cells using a coin-type cell. The absolute initial charge capacities of the systems were similar, supporting that the depth of initial lithiation into Si anode is also very similar, 148.14 mAh/g_{LCO} (3.14 ± 0.025 mAh) for the LCO system, 177.42 mAh/g_{NMC532} (2.87 ± 0.046 mAh) for the NMC532 system, and 148.81 mAh/g_{LFP} (2.76 ± 0.12 mAh) for the LFP system.

However, after three formation cycles (Fig. S2a–c), each cell system displays different capacity fade rates (see Fig. 1a). For the LFP system, the capacity fade is a linear function of cycle number. On the other hand, for the LCO system, capacity fade follows a linear-with-cycle-count rate law until ~15 cycles have been accrued. At ~15 cycles, the fading rate suddenly displayed an exponential increase. The coulombic efficiencies, shown in Fig. 1b, also display a similar change at ~15 cycles. The efficiency of the LCO system becomes a very unstable after ~30 cycles, possibly

because of reactions of the electrolyte with the surface of the electrode material. The coulombic efficiency of the LFP system is the most stable, and higher than the other two during all 50 cycles of cycle life test. The change in the capacity fade rate in the LCO cycling experiments indicates a change in fade mechanism.

To better understand the different capacity-fading behaviors of each system, we further conducted a three-electrode test to demonstrate the different degradation of the Si anodes. Fig. 1d–f shows differential capacity vs. voltage curves (dQ/dV) of Si vs. the Li reference electrode during lithiation/delithiation of formation process (C/20) and cycle life test (C/3). During formation process, the curves from all systems show two lithiation peaks, L1(a-Si to a-Li_{2.0}Si) and L2 (a-Li_{2.0}Si to a-Li_{3.5}Si), and two delithiation peaks, D1 (a-Li_{2.0}Si to a-Si) and D2 (a-Li_{3.5}Si to a-Li_{2.0}Si). The L2 peak is more clearly observed in the LFP system, and this would imply that less polarization is applied on Si in the LFP system. During cycle life test, electrochemistry of Si more clearly differs from one another. For Si in the NMC532 or LFP system, the intensities of L2 and D2 peaks decrease as a function of cycle number due to gradual Li loss, while L1 and D1 peaks are relatively stable. On the other hand, for Si in the LCO system, all lithiation/delithiation peaks rapidly degrade. This implies that not only Li loss but also loss of active Si occurs in the LCO system. The optical images of the Si anodes harvested from each system after 50 cycles (Fig. 1f) support this idea that severe loss of Si (delamination) occurred in the LCO systems.

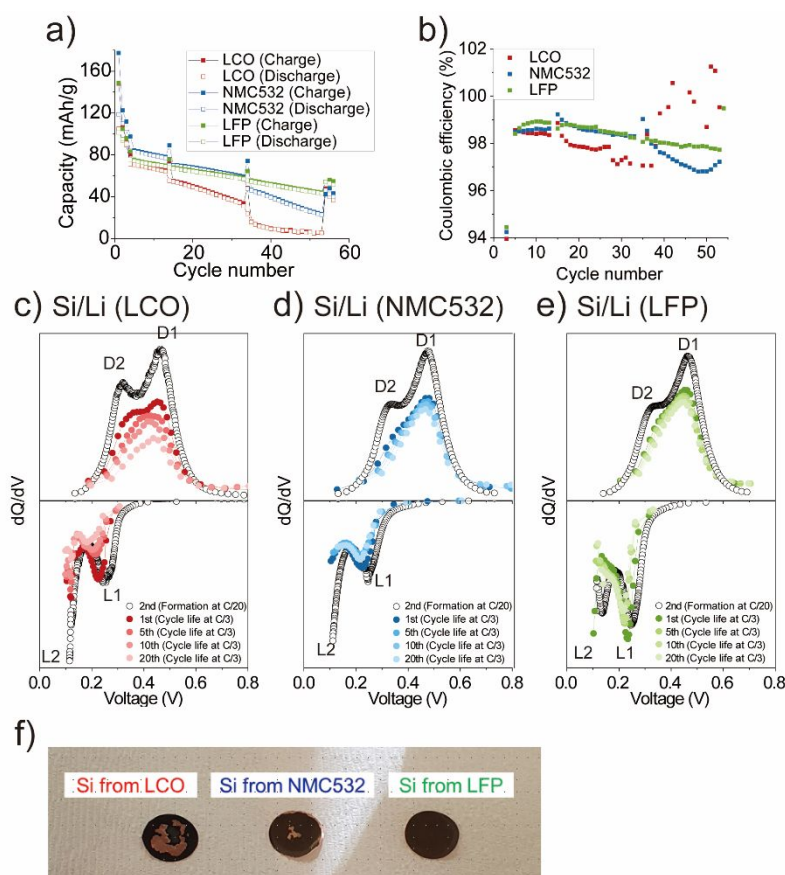


Figure 1. Electrochemical properties of the LCO, NMC532, and LFP systems. a) Plot of charge/discharge capacity (mAh/g_{cathode}) vs. cycle number and b) Coulombic efficiency of each system. c–d) Differential capacity vs. voltage curves of Si vs. Li reference from three-electrode cells, during lithiation/delithiation of formation (C/20) and cycle life test (C/3): c) LCO system, d) NMC532 system, e) LFP system. f) Optical images of harvested Si anodes from each system (coin cell) after cycle life test.

2.2. The effect of crosstalk on the degradation mechanism of the Si anode during cycling

2.2.1. The effect on the formation mechanism of Si SEI in each system

Since the only difference among the systems studied is in the cathode materials, we compared the crosstalk behavior in each one to understand the impact of the cathode material on the degradation of the Si anode. We compared the mechanisms of electrolyte decomposition by using linear sweep voltammetry (LSV), as shown in Fig. 2a. The voltage vs. current plots show

one large peak, which corresponds to a main electrolyte decomposition reaction in each system (enlarged in blue dashed box in Fig. 2a). Interestingly, the corresponding potentials of these peaks in each system differ: 3.42 V for LCO, 3.23 V for NMC532, and 3.12 V for LFP. In addition to the main current peaks, several minor ones can also be observed in the lower-potential region (enlarged in red dashed box in Fig. 2a), and the corresponding potentials for these peaks are also different. These observations support the idea that electrolytes in the three systems decompose in different ways. Given that the cathode materials used in this study have different transition metal ions, metal oxidation states, and surface chemistry (layered for LCO and NMC532 vs. olivine for LFP), these properties can affect interphase reactions between cathodes and electrolytes and can affect electrolyte decomposition reactions.²⁵⁻³³ For example, transition metal ions in each cathode have different oxidizing ability, which could affect the mechanism and kinetics of electrolyte decomposition; the expected trend would be Ni (IV) > Co (IV) > Fe (III).

The different decomposition reactions of the electrolyte affect the SEI formation mechanism on the Si anode (Fig. 2b–d, Figures. S3–S5). Fig. 2b shows the concentration of what could be organic carbonate species (C-O, C=O, O-C=O) in C 1s spectra on the harvested Si anodes, as a function of potential. Since organic carbonate species form because of solvent decomposition, the concentration would imply the extent of solvent decomposition in each system. The samples from the LFP system show that the concentration decreases as a function of potential, which means that the Si SEI formed at lower potential (<2.5V) well passivates the surface of the Si anode, suppressing the further decomposition reaction of organic solvents in the higher potential range (>2.5V). While the samples from both LCO and NMC532 systems show the opposite trend from the LFP system. The concentrations gradually increase as a function of potential. The samples from LCO system show the highest value of an average concentration (~23%) in an entire potential range, compared with the others (NMC532 system: 18%, LFP system: 15.6%). This implies that organic solvent decomposition would be the most prevalent in the LCO system.

The reactions related to salt (LiPF₆) decomposition are also different in each system, forming different inorganic decomposition species on the SEI of Si anodes (Fig. 2c and 2d). For all systems, the decomposition of LiPF₆ forms Li_xPO_y and Li_xPO_yF_z-based species in the low potential range. However, the main decomposition species in each system differently change as potential increases. For the LCO system, the concentration of Li_xPO_yF_z-based species suddenly

drops at 3.0V, making, LiF and Li_xPO_y species the main decomposition compounds at $>3.0\text{V}$. While in the NMC532 system, LiF and $\text{Li}_x\text{PO}_y\text{F}_z$ -based compounds are the main decomposition species on the SEI of Si anodes. Interestingly, for the LFP system, the concentration of LiF suddenly increases at 2.5V and the concentration of the others drops to 0% at 3.2V, making LiF the only observed decomposition compounds. These results support the idea that the different formation mechanism of SEI on each Si anode is not simply because of cell potential, but, rather, it is a result of the effect of cathode crosstalk.

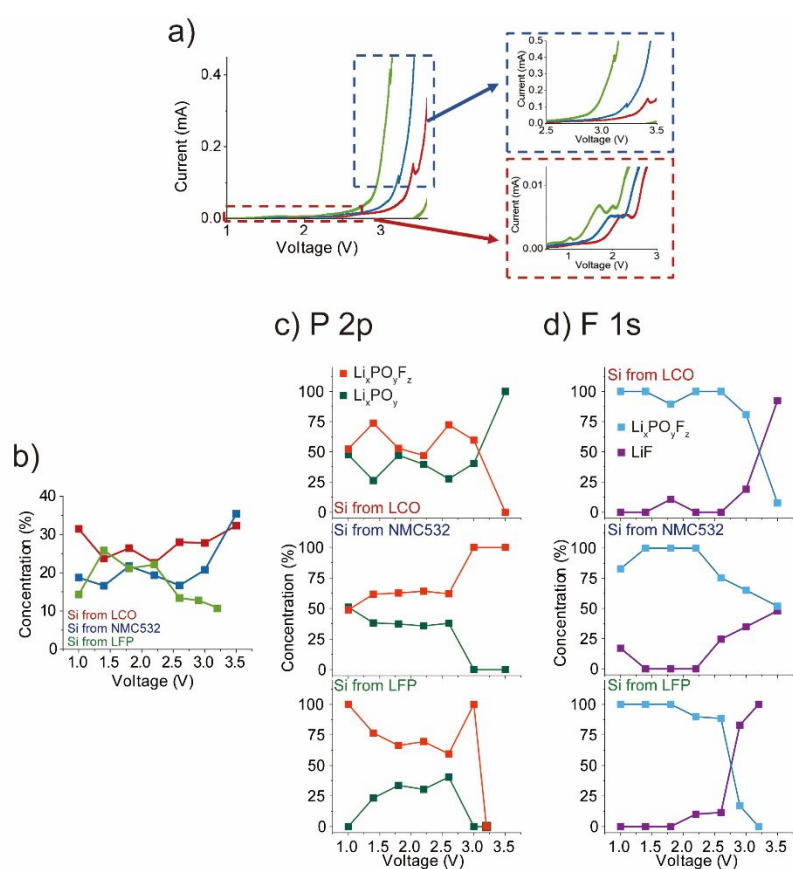


Figure 2. a) Current vs. voltage from linear sweep voltammetry of the LCO, NMC532, and LFP systems. XPS analysis of harvested Si anodes from each system, as a function of potential. b) The concentration of what could be organic carbonate species (C-O, C=O, O-C=O) in C 1s, observed in Fig. S4. The concentration of the species observed in the c) P 2p spectra (Fig. S5) and d) F 1s spectra (Fig. S6). Color code: green in Fig. 2c: Li_xPO_y , red in Fig. 2c: $\text{Li}_x\text{PO}_y\text{F}_z$, purple in Fig. 2d: LiF, blue in Fig. 2d: $\text{Li}_x\text{PO}_y\text{F}_z$

2.2.2. The effect of crosstalk in the early stages of performance degradation

To understand how the crosstalk behavior manifests itself as a function of cycle number, we performed post-mortem analysis on aged electrolytes and Si electrodes. Fig. 3a shows HPLC results, showing total-ion chromatograms (TICs) of the aged electrolytes extracted from the three full-cell systems, after 2 cycles of cycle life test at the C/3 rate. Compared to the fresh electrolyte (Gen2 electrolyte, details are in experimental section), multiple new peaks can be observed in the TICs of the aged electrolytes (Fig. 3a), indicating the formation of new organic compounds during cycling. The new peaks were assigned to several compounds, designated by their molecular weight (M.W.), given as 200, 228, 256, 236, 242, 250, 256, 288, 270, and 294 g/mol, respectively, in Table 1. Overall, the TICs look similar and contain most of the same characteristic peaks. However, their intensities are quite different. The proposed chemical structures for each compound are given in Fig. 4, and their single-ion chromatograms (SICs) are displayed in Fig. S6. The method used to propose the chemical structures is explained in a previous publication.¹⁸ Interestingly, these species likely contain C=C or C-F bonds, which were observed before as crosstalk species.¹⁸

Since peak intensity in mass spectrometry is linear with concentration, the relative areas of the peaks in the SICs were used as surrogates for the species' concentration. Table 1 and Fig. 3c–e show that the relative areas of electrolyte decomposition products are sensitive to the nature of the cathode material. The fact that some of the compounds are seen in the uncycled Gen2 electrolyte, and their concentrations decrease differently with aging, which may indicate that these products are consumed in different ways. The LCO system shows the most significant decrease after 2 cycles. This implies that electrolyte decomposition in the LCO system occurred extensively in the early stages of cycling, as we expected in the previous results about a significant decomposition reaction of solvent in the LCO system (Fig. 2b).

Table 1. Most intense peaks in the aged electrolyte after 2 cycles of cycle life test at the C/3 rate.

Compound/empirical formula	Adduct	m/z, Da	M.W, g/mol	Uncycled Gen2 electrolyte: Relative peak area (%)	SIC	LCO: Relative SIC peak area (%)	NMC532: Relative SIC peak area (%)	LFP: Relative SIC peak area (%)
EC(Ethylene carbonate)	H ⁺	89	88	35.03				
[C ₅ H ₈ O ₄ PF ₂][H ⁺	H ⁺	201	200			3.73	3.10	6.89
[C ₅ H ₉ O ₆ PF][H ⁺	H ⁺	215	214	23.75		8.11	14.87	13.59
[C ₈ H ₁₄ O ₆][Na ⁺	Na ⁺	229	206	31.11		13.82	28.35	20.53
[C ₆ H ₁₃ O ₇ P][Na ⁺	Na ⁺	251	228			0.90	0.26	0.30
[C ₇ H ₁₁ O ₇ PF][H ⁺	H ⁺	257	256			3.32	6.21	5.45
[C ₈ H ₁₀ O ₅ PF][Na ⁺	Na ⁺	259	236			1.30	1.27	2.95
[C ₇ H ₁₂ O ₆ PF][Na ⁺	Na ⁺	265	242			3.04	3.90	1.68
[C ₈ H ₁₁ O ₇ P][Na ⁺	Na ⁺	273	250			3.12	2.99	2.87
[C ₇ H ₁₃ O ₈ P][Na ⁺	Na ⁺	279	256			11.75	9.30	4.90
[C ₈ H ₁₂ O ₇ PF ₂][H ⁺	H ⁺	289	288			6.22	1.63	7.35
[C ₈ H ₁₂ O ₇ PF][Na ⁺	Na ⁺	293	270			16.09	8.33	3.40
[C ₇ H ₁₃ O ₆ PF ₃][H ⁺ /Na ⁺	H ⁺ /Na ⁺	281/303	280	10.12		12.88	8.04	15.05
[C ₈ H ₁₂ O ₅ PF ₄][H ⁺ /Na ⁺	H ⁺ /Na ⁺	295/317	294			15.73	11.74	15.03

With these crosstalk behaviors, the SEI layers in each system grow in a different way. The XPS results from the three harvested Si anodes after 2 cycles (Si_{LCO_2} , $\text{Si}_{\text{NMC532}_2}$, Si_{LFP_2}) show that the atomic concentrations vary in each sample, as shown in Fig. 5a-b. Comparing the results from Si_{LCO_2} and $\text{Si}_{\text{NMC532}_2}$ with those from Si_{LFP_2} shows that the concentrations of fluorine are higher and the concentrations of carbon and oxygen are lower in the Si_{LFP_2} than in the Si_{LCO_2} and $\text{Si}_{\text{NMC532}_2}$. This finding supports the idea that Si_{LFP_2} has an SEI rich in inorganic species, which is more robust and stable. Also, analysis of F 1s and P 2p spectra (Fig. 5c-d) shows that the SEI layer on Si from both the LCO and NMC532 systems consists of high concentrations of Li_xPO_y (Si_{LCO_2}) or $\text{Li}_x\text{PO}_y\text{F}_z$ -based species ($\text{Si}_{\text{NMC532}_2}$), whereas, SEI of Si_{LFP_2} has a very high concentration of LiF, which has been widely understood as an SEI stabilizer.^{22, 34}

Different crosstalk behaviors have an impact on state of health of Si in each system, even after 2 cycles of cycle life test at C/3. To demonstrate this point, we assembled half-cells with the harvested Si anodes, which are hereafter called Si_{LCO_2} half-cell, $\text{Si}_{\text{NMC532}_2}$ half-cell, and Si_{LFP_2} half-cell. Fig. 6a shows the capacity vs. voltage curves of each harvested Si half-cell during the first and second cycle at the C/20 rate between 0.01 V and 1.5 V. All the half-cells have similar

first lithiation capacities (Fig. 6a, Table S1). This means that there was no significant difference among the systems in the loss of active Si during 2vcycles of cycle life test at C/3, in the full-cells. In contrast, the half-cells differ greatly in delithiation behavior. For the Si_{LCO_2} half-cell, the voltages rapidly increase, and the delithiation capacity is only 1554 mAh/g_{Si}; this half-cell exhibits a coulombic efficiency of only 67%. Afterwards, the cell shows a huge decrease in the second lithiation capacity (1359 mAh/g_{Si}), suggesting that a large loss of active Si occurred during the first delithiation. While the Si_{LFP_2} half-cell shows a coulombic efficiency of 93%. The dQ/dV curves also clearly reveal the differences in the electrochemistry of each Si anode is a result of different phase evolution in late stage of delithiation (Fig. 6b). All cells show clear D2 peak, corresponding to the phase transformation from a-Li_{3.5}Si to a-Li_{2.0}Si, while there is a noticeable difference in peaks at later stage of delithiation. For the Si_{LCO_2} half-cell, the D1 delithiation peak, which corresponds to the phase transformation from a-Li_{2.0}Si to a-Si, is rarely observed. In contrast, its intensity is very strong in the Si_{LFP_2} half-cell. Also, another sharp peak (D3), which corresponds to the delithiation of the c-Li₁₅Si₄ phase, can only be observed in the Si_{LFP_2} half-cell. In general, large mechanical changes, such as stress and fractures, develop at the late stage of delithiation, and they could result in SEI breakage and rapid degradation of Si.^{5, 35-37} Therefore, the mechanical stability of SEI, which can compensate and/or tolerate the large mechanical changes, is very important factor for reversible phase transformation of the Si anode. In this regard, only Si_{LFP_2} half-cell clearly displays reversible phase transformations showing both D1 and D3 peaks, which means that SEI of Si_{LFP_2} is mechanically stable. This would be because that SEI layer on the Si_{LFP_2} mainly consisting of inorganic species and LiF, which have been widely understood as mechanical more stable components.^{22, 34} While it appears that the SEI of Si_{LCO_2} and Si_{NMC532_2} are rich in organic species, Li_xPO_y and/or Li_xPO_yF_z and, therefore, not stable, the phase transformation is not reversible in both Si_{LCO_2}– and Si_{NMC532_2} half cells.

The difference in Si SEI layer stability in the harvested Si samples is also reflected in the extent of Li loss in the cathode. In Si-based batteries, SEI breakage due to mechanical failure of Si anode easily occurs, leading to consistent consumption of Li for re-construction of SEI, and this is one of the most important issues in Si-based Li ion batteries. To check this point, we assembled half-cells with the fresh cathodes (Cathode_{LCO_fresh} half-cell, Cathode_{NMC532_fresh} half-cell, and Cathode_{LFP_fresh} half-cell, respectively), and half-cells with harvested cathodes extracted from each system after 2 cycles (Cathode_{LCO_2} half-cell, Cathode_{NMC532_2} half-cell, and Cathode_{LFP_2} half-cell,

respectively). Fig. S7a-c shows the capacity vs. voltage curves of these six half-cells at $C/20$. Since the data were obtained at the very slow, $C/20$ rate, we could neglect the impedance effect but focus on Li inventory of each cathode. The first charge capacities of all cells with the harvested cathodes are very small compared to those with fresh cathodes, which means that there was a large loss of active Li, most likely due to reconstruction of the SEI. The LFP system shows the most moderate Li loss than the LCO or NMC532 systems (LCO: 1.695 mAh, NMC532: 1.215 mAh, LFP: 1.025 mAh in Fig. 7a), and this would be because that the stable SEI of Si_{LFP_2} would well prevent SEI breakage during repeated charge/discharge processes. After the first cycle, all harvested cathodes (red solid line in Fig. S7a-c) from the three systems work as if they were fresh cathodes (red dashed line in Fig. S7a-c).

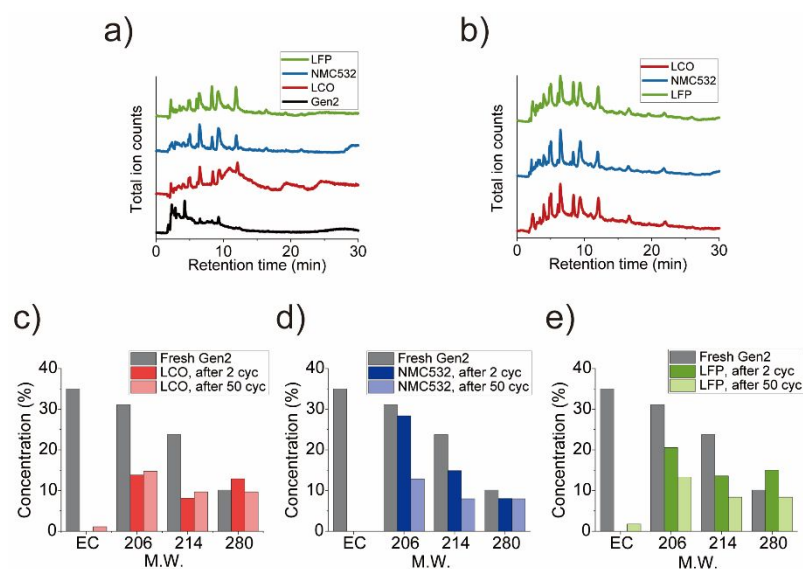


Figure 3. a) Total-ion chromatograms of uncycled Gen2 electrolyte and the aged electrolytes, extracted from each system after the initial 2 cycles at the $C/3$ rate. b) Total-ion chromatograms of the aged electrolytes extracted from each system after 50 cycles at the $C/3$ rate. c–e) Comparisons of the concentrations of specific compounds (EC, M.W.=206, 214, 280) in the fresh Gen2 electrolyte and in the aged electrolyte from the c) LCO, d) NMC532, e) LFP system.

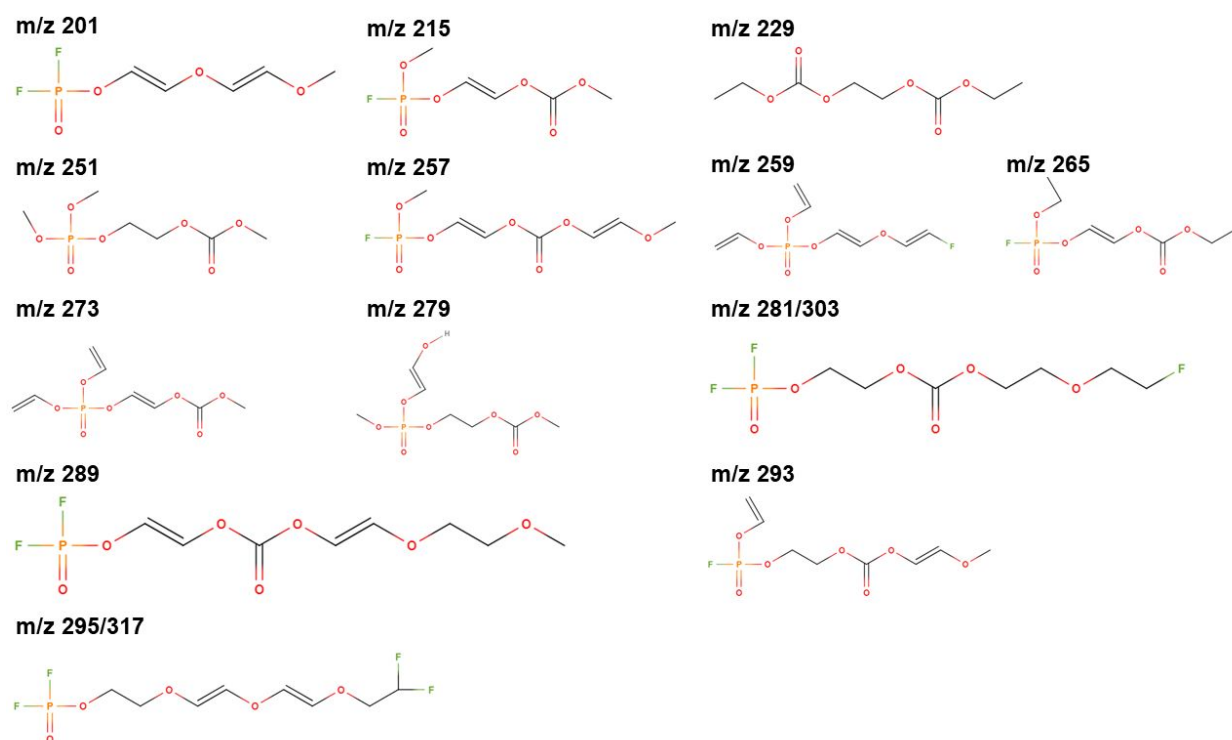


Figure 4. Proposed chemical structures of compounds detected by HPLC/MS-ESI.

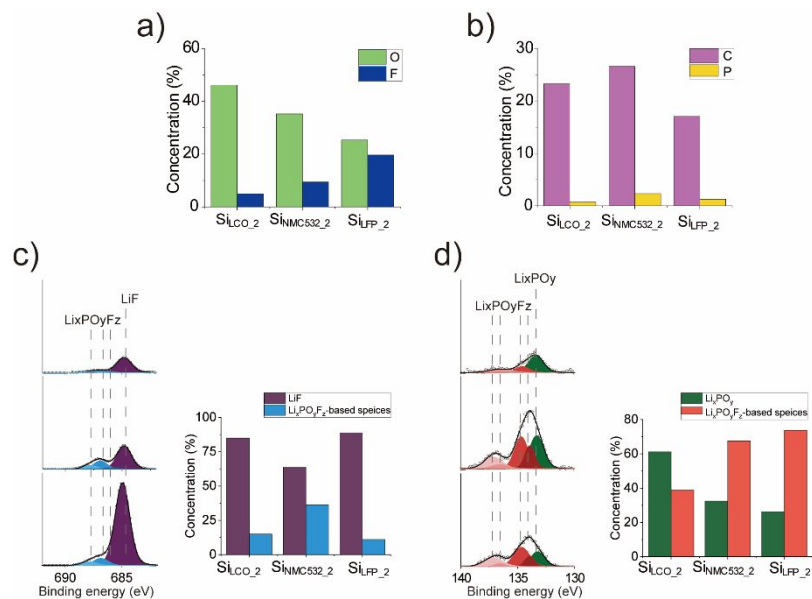


Figure 5. XPS analysis of the harvested Si anodes from each system, after the initial 2 cycles at the C/3 rate. a) atomic concentrations of O, F and b) C, P on the surfaces of the harvested electrodes. c) F 1s spectra and the relative concentration of the observed species. d) P 2p spectra and the relative concentration of the observed species. The Li_xPO_yF_z concentrations are the sum of all Li_xPO_yF_z-based species in Fig. 5c-d.

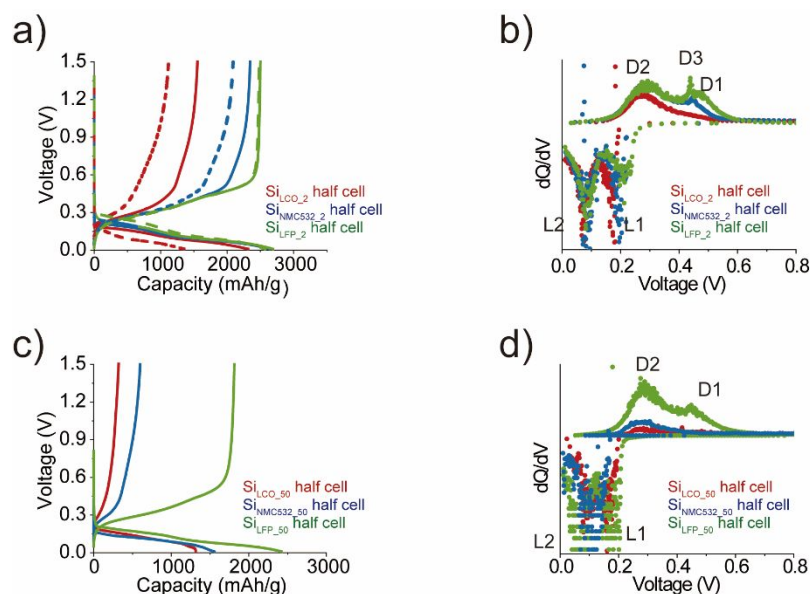


Figure 6. Electrochemical properties of the harvested Si from each system, after the 2 cycles of cycle life test at the C/3 rate. a) Voltage profiles and b) differential capacity vs. voltage curves of the harvested Si anode/Li half-cells. Solid lines represent the first cycle; dashed lines represent the second cycle. Color code for figures 6a and 6b: red, Si_{LCO}₂ half-cell; blue, Si_{NMC532}₂ half-cell; green, Si_{LFP}₂ half-cell. **Electrochemical properties of the harvested Si from each system, after 50 cycles of cycle life test at the C/3 rate.** c) Voltage profiles and d) differential capacity vs. voltage curves of the harvested Si anode/Li half-cells. Color code for figures 6c and 6d: red, Si_{LCO}₅₀ half-cell; blue, Si_{NMC532}₅₀ half-cell; green, Si_{LFP}₅₀ half-cell.

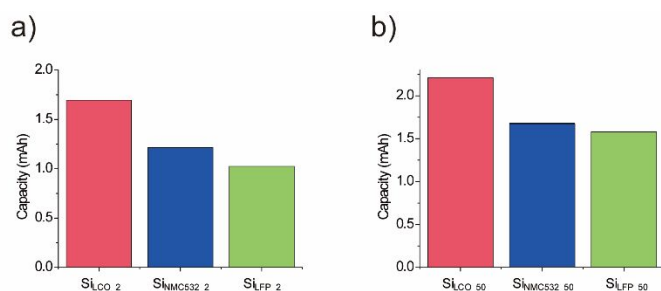


Figure 7. The amount of Li loss, a) after 2 cycles of cycle life test at C/3, b) after 50 cycles of cycle life test at C/3. Capacity loss is defined as the difference in the 2nd charge capacity between fresh and harvested cathode half-cells in Fig. S7.

2.2.3. The effect of crosstalk on the later stages of performance degradation

The crosstalk behaviors become more apparent after 50 cycles. Fig. 3b shows the TICs of the aged electrolyte extracted from the three systems, after 50 cycles of cycle life test at the C/3 rate. The most intense compounds in each aged electrolyte are summarized in Table 2, and the SICs of the compounds are shown in Fig. S8. As shown in Fig. 3c–e, the compounds observed in the fresh Gen2 electrolyte (M.W.=214, 206, 280) decreased further in all samples. However, for the LCO system, the relative amounts of decomposition products did not change between cycle 2 and cycle 50 because most of the decomposition reactions had already occurred in the early stages of cycle life. In contrast, the relative amounts of decomposition products gradually change in the LFP system. These differences are shown in Table 2.

The differences in SEI growth mechanism of each Si anode becomes more apparent after 50 cycles. Fig. 8 shows SEI chemistry in the harvested Si anodes from each system ($\text{Si}_{\text{LCO}_50}$, $\text{Si}_{\text{NMC532}_50}$, $\text{Si}_{\text{LFP}_50}$). Even after 50 cycles, SEI of $\text{Si}_{\text{LCO}_50}$ and $\text{Si}_{\text{NMC532}_50}$ does not change much. Both Si anodes still have SEIs rich in organic species with high concentrations in oxygen, and low concentration in fluorine. The concentration of Li_xPO_y species is the highest in $\text{Si}_{\text{LCO}_50}$ and the concentration of $\text{Li}_x\text{PO}_y\text{F}_z$ -based species is the highest in $\text{Si}_{\text{NMC532}_50}$. Whereas, Si SEI of $\text{Si}_{\text{LFP}_50}$ changes to a SEI rich in organic species after 50 cycles; oxygen concentration significantly increases (Oxygen: 25.3% to 44.5%) but the fluorine concentration decreases (19.6% to 4.1%). By combining the XPS results of each Si SEI chemistry as a function of cycle numbers, we summarize a SEI formation and growth mechanism of Si anodes in each system (Fig. 8d). For Si anodes in the LCO or NMC532 systems, Si SEI layers rich in organic species with high concentration of Li_xPO_y (LCO system) or $\text{Li}_x\text{PO}_y\text{F}_z$ -based species (NMC532 system) form and grow throughout the whole cycle life test. While, for the Si anode in the LFP system, Si SEI rich in inorganics with a high concentration of LiF, which is robust and stable form at the early stage of cycling, and then SEI layers rich in organic species grow as cycle number increases. Therefore, Si SEI in the LFP system consists of two different layers; bottom: inorganic/LiF-rich layer, top: organic-rich layer.

Also, since the LFP system was cycled between voltage limits that were different from the other two systems, we investigated the effect of voltage limits on the Si SEI layer of each system (Fig. S9). Here, we tested the LCO and NMC532 systems between the voltage limits of 2.7 and 3.7 V for 50 cycles, and performed XPS on the harvested Si anodes from both systems

(Si_{LCO_3.7V_50}, Si_{NMC532_3.7V_50}). The results show that the concentrations of Li_xPO_y- or Li_xPO_yF_z-based species in both samples are significantly larger than those seen in Si_{LFP_50}, supporting the idea that the different decomposition reaction of LiPF₆ still occurs significantly in both LCO and NMC532 systems within the narrower voltage limits. Therefore, the effect of voltage limits on Si SEI chemistry appears to be insignificant.

With these different cathode effects on crosstalk, each cell systems displayed different aging behaviors after 50 cycles. The electrochemical performances of the half-cells with the harvested Si extracted after 50 cycles in full cells, Si_{LCO_50} half-cell, Si_{NMC532_50} half-cell, and Si_{LFP_50} half-cell are presented in Figs. 6c-d and Table S3. There is a significant loss of active Si in both the LCO and the NMC532 system after 50 cycles of cycle life test. For example, the Si_{LCO_50} half-cell (1315 mAh/g_{Si}) and Si_{NMC532_50} half-cell (1554 mAh/g_{Si}) show a significant capacity loss in their first lithiation, compared to that of the Si_{LCO_2} or Si_{NMC532_2} half-cell. In contrast, the Si_{LFP} half-cell shows a first lithiation capacity of 2420 mAh/g_{Si}, meaning that the loss of active Si in this case was not as severe as in the other cases. In addition, the Si_{LCO_50} and Si_{NMC532_50} half-cells also show very low coulombic efficiency (24% and 38.5%, respectively) and very weak D1 and D2 peaks (Fig. 6d), whereas the Si_{LFP_50} half-cell shows relatively strong D1 and D2 peaks (Fig. 6d), and its coulombic efficiency is the highest (75%, Table S3).

As the cycle count increased, Li loss also increased. However, it was greater in the LCO and NMC532 systems as compared to the LFP system (Fig. 7b, Fig S7d-f and Table S4). For the LCO system, the capacity loss (cyclable Li) is 2.209 mAh, but it is 1.579 mAh in the LFP system. Interestingly, all harvested cathodes from the three systems work as if they were fresh cathode. This finding supports the idea that the degradation of the cathode is not the main source of the performance decline observed in the Si full cells even after 50 cycles.

Table 2. Most intense peaks in the aged electrolyte after 50 cycles of cycle life test at the C/3 rate.

	Adduct	m/z	M.W.	LCO: Relative SIC peak area (%)	NMC532: Relative SIC peak area (%)	LFP: Relative SIC peak area (%)
EC	H ⁺	89	88	1.09	0.00	1.78
[C ₅ H ₈ O ₄ PF ₂] ⁺ H ⁺	H ⁺	201	200	4.54	3.12	4.74
[C ₅ H ₉ O ₆ PF] ⁺ H ⁺	H ⁺	215	214	9.67	7.96	8.36
[C ₈ H ₁₄ O ₆] ⁺ Na ⁺	Na ⁺	229	206	14.77	12.87	13.35
[C ₆ H ₁₃ O ₇ P] ⁺ Na ⁺	Na ⁺	251	228	2.29	0.94	0.83

$[\text{C}_7\text{H}_{11}\text{O}_7\text{PF}]\text{H}^+$	H^+	257	256	7.38	7.48	8.31
$[\text{C}_8\text{H}_{10}\text{O}_5\text{PF}]\text{Na}^+$	Na^+	259	236	4.46	7.57	8.67
$[\text{C}_7\text{H}_{12}\text{O}_6\text{PF}]\text{Na}^+$	Na^+	265	242	7.25	7.56	4.97
$[\text{C}_8\text{H}_{11}\text{O}_7\text{P}]\text{Na}^+$	Na^+	273	250	4.62	8.56	8.08
$[\text{C}_7\text{H}_{13}\text{O}_8\text{P}]\text{Na}^+$	Na^+	279	256	12.36	14.35	9.00
$[\text{C}_8\text{H}_{12}\text{O}_7\text{PF}_2]\text{H}^+$	H^+	289	288	3.08	1.67	3.41
$[\text{C}_8\text{H}_{12}\text{O}_7\text{PF}]\text{Na}^+$	Na^+	293	270	7.74	11.39	5.72
$[\text{C}_7\text{H}_{13}\text{O}_6\text{PF}_3]\text{H}^+/\text{Na}^+$	H^+/Na^+	281/303	280	8.35	5.99	9.59
$[\text{C}_8\text{H}_{12}\text{O}_5\text{PF}_4]\text{H}^+/\text{Na}^+$	H^+/Na^+	295/317	294	12.40	10.52	13.19

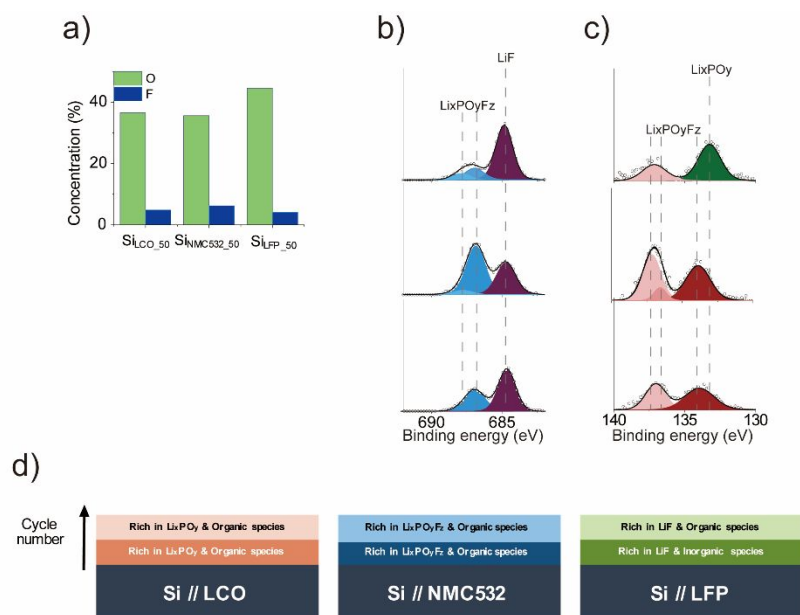


Figure 8. XPS analysis of the harvested Si anodes from each system after 50 cycles at C/3. a) atomic concentrations of O and F on the surfaces of the harvested electrodes. b) F 1s and c) P 2p spectra of the harvested Si anodes. d) Schematic of the SEI growth mechanism on Si anodes from each system.

2.3 Correlations between the XPS and HPLC data

Many electrolyte decomposition reactions have been reported in the literature.³⁸⁻⁴³ Most involve the reduction of one or more of the components in the electrolyte, forming lithium-bearing species. However, the connection between some of these products and the composition of the SEI layer on the negative electrode has only been inferred. If the electrolyte decomposition reaction were to occur, for example, as shown schematically in Eq. 1, then there should be a strong correlation between the soluble organophosphorus and the insoluble inorganic species.

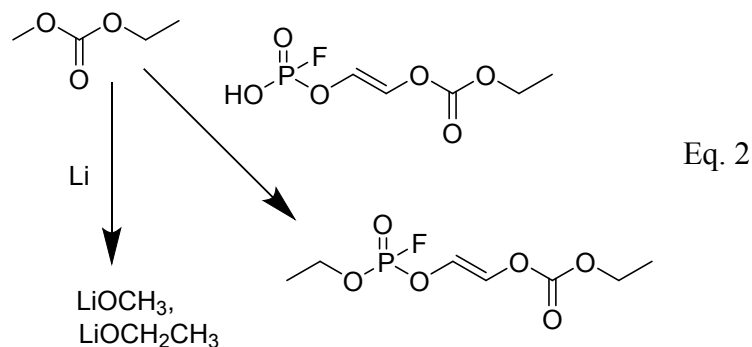


Analogous reasoning can be used to understand the relationship between soluble species and XPS organic environments seen on the surface of the negative electrode material. Table 3 shows the calculated correlations between the relative amounts of species detected in the HPLC and those observed by XPS where the absolute value of the correlation coefficient was 0.95 or greater. Some of the correlation coefficients in Table 3 are negative. Statistically speaking, a negative correlation coefficient suggests that the two data sets being compared are inversely related. That is, in one set, y increases with x , while in the other, y decreases as x increases. In a chemical process, an inverse relationship is usually found in a system of competing reactions, such as that that may lead to the relationship given in the sixth line of Table 3. We propose the organophosphate shown in Eq. 2 to represent the empirical formula shown in the table. For the scenario shown in Eq. 2, two reactions are competing for the same starting material, ethyl methyl carbonate. One reaction is the reduction by lithium from the negative electrode to form alkoxide anions from ethyl methyl carbonate (EMC), the LiO-C group of which could be detected by the XPS. A large, negative correlation coefficient, such as that between LiF and $[\text{C}_8\text{H}_{12}\text{O}_7\text{PF}]\text{Na}^+$ (see Table 3), may indicate that the reactions leading to LiF and to $\text{C}_8\text{H}_{12}\text{O}_7\text{PF}$ may be competing for the same material, such as the LiPF_6 salt in the electrolyte. The other pathway, occurring somewhere else in the cell, is transesterification with an organophosphate, forming a new compound that may be the species detected in the HPLC experiment.

Table 3. Correlations between the HPLC and XPS data.

Cycle count	XPS spectrum	HPLC species	XPS chemical environment	Correlation coefficient
2	F1s	$[\text{C}_8\text{H}_{12}\text{O}_7\text{PF}]\text{Na}^+$	LiF	-0.99
2	F1s	$[\text{C}_7\text{H}_{13}\text{O}_6\text{PF}_3]\text{H}^+/\text{Na}^+$	LiF	-0.99
2	P2p	$[\text{C}_8\text{H}_{12}\text{O}_7\text{PF}]\text{Na}^+$	Li_xPO_y	0.97
2	P2p	$[\text{C}_7\text{H}_{13}\text{O}_6\text{PF}_3]\text{H}^+/\text{Na}^+$	$\text{Li}_x\text{PO}_y\text{F}_z$	-0.99
2	C1s	$[\text{C}_7\text{H}_{12}\text{O}_6\text{PF}]\text{Na}^+$	C-O, C-O-C	-0.99

2	C1s	$[\text{C}_5\text{H}_8\text{O}_4\text{PF}_2]\text{H}^+$	O-C=O	>0.99
2	C1s	$[\text{C}_7\text{H}_{12}\text{O}_6\text{PF}]\text{Na}^+$	O-C=O	0.98
50	C1s	$[\text{C}_7\text{H}_{13}\text{O}_8\text{P}]\text{Na}^+$	O-C=O	0.96
50	C1s	$[\text{C}_8\text{H}_{11}\text{O}_7\text{P}]\text{Na}^+$	O-C(=O)O	>0.99



3. Conclusion

We systemically investigated the crosstalk behavior in Si-based full cells using three different cathode materials, LCO, NMC532, and LFP. The decomposition reaction of electrolyte in the LCO or NMC532 system mainly occurred at the early stage of cycle life, whereas it occurred gradually in the LFP system. Because of this difference, the formation and growth mechanism of the SEI layer was found to be very sensitive to the nature of the cathode material. Noteworthy, for the LFP system, Si SEI rich in LiF and inorganic species, which is stable and robust forms at the early stage of cycle. As a result of this behavior, mechanical failure of the Si electrode and lithium loss are well suppressed in the LFP system, preventing rapid capacity fading. Therefore, the results show that crosstalk can have a great impact on performance degradation in Si full cells.

4. Experimental

Materials. All electrodes used in this study were made at the Cell Analysis, Modeling, and Prototyping (CAMP) Facility at Argonne National Laboratory. Their compositions are given in Table 4.

Table 4. Composition and characteristics of electrodes.

	Si	LCO	NMC532	LFP
Active material	80 wt% Si (Paraclete Energy)	90 wt% NMC532 (BTR)	90 wt% NMC532 (Toda)	90 wt% LFP (Jonson Matthey)
Binder	10 wt% lithium polyacrylate	5 wt% Polyvinylidene fluoride (PVDF, Solvay 5130)	5 wt% PVDF	5 wt% PVDF
Conducting agent	10 wt% Timcal C45 carbon	5 wt% Timcal C45 carbon	5 wt% Timcal C45 carbon	5 wt% Timcal C45 carbon
Loading density (mg/cm ²)	0.96	14.5	11.4	13.4

Cell (dis)assembly and testing. The data in Fig 1c-e and Fig S1 were obtained from three-electrode Swagelok® ‘T’-cells. The other cycling data were obtained from coin cells (CR2032). The Si anodes were cut into 15-mm-diameter disks, and cathode electrodes were cut into 14-mm diameter disks. The Si anodes were dried at 140°C for 12 h, and cathodes were dried at 110°C for 12h. All electrodes were dried *in vacuo*. The composition of the electrolyte was 1.2 M lithium hexafluorophosphate in ethylene carbonate:ethyl methyl carbonate (3:7 by wt, Gen2 electrolyte). The Gen2 electrolyte was purchased from Tomiyama Pure Chemical Industries. Celgard® 2325 was used as the separator, and it was cut into 16-mm-diameter disks. The cells were assembled in an argon-filled glovebox. A MACCOR Series 4000 Battery Tester was used to perform the cell cycling. The voltage window for the LCO and NMC532 systems was 3.0 V–4.1 V, and for the LFP it was 2.7 V–3.7 V. The cells were formed using three charge-and-discharge cycles at the C/20 rate. After formation, the cells were cycled at the C/3 rate for 50 cycles. The hybrid pulse power characterization tests were conducted after formation; after 10 cycles; after 30 cycles; and at the end of the cycling test. All results are averages of three cells for each system. For the linear

sweep voltammetry (LSV) test in Fig. 2a, we prepared the same coin cell described in the previous paragraph, and the test was performed using an AMETEK® Solartron® 8-channel cell test system (Model 1470E) that was operated by the vendor-provided MultiStat® software. The scan rate was 1 mV/s.

For the three-electrode tests (Fig. 1c-e and Fig. S1), the cathodes and Si electrodes were cut into 11-mm-dia (7/16-in.) disks. The Si anodes were dried under 140°C for 12 h, and cathodes were dried under 110°C for 12 h. Inside an Ar-atmosphere glovebox, they were assembled into three-electrode, Swagelok® 'T'-cells, as shown schematically in Fig. S10. Two layers of 30- μ m-thick non-woven glass mats were used as a separator between cathodes and Si anodes, and an additional two layers of 420- μ m-thick, 12.5-mm-dia (Whatman GF/F) disks were used as a separator between active electrodes and the Li reference electrode. The glass mats were then dried *in vacuo* for 4 h at 120°C before cell assembly. Compression springs (Gardner Spring GC360-032-0500-S) were used to maintain pressure on the electrochemical components. Gen2 electrolyte was also used for this study. The electrochemical measurements were again performed using an AMETEK® Solartron® 8-channel cell test system (Model 1470E) that was controlled by the vendor-provided MultiStat® software. The voltage window was 3.0 V–4.1 V for the LCO and NMC532 systems and 2.7 V–3.7 V for the LFP system. Formation consisted of three charge-and-discharge cycles at the C/20 rate. The cells were cycled at the C/3 rate for 20 cycles.

To study Si SEI layer chemistry as a function of potential (Fig. 2b–g, Figs. S3–S5), we prepared several coin cells from each system, which were galvanostatically charged at the C/40 rate to the desired cutoff voltage. The cells were then held at the desired voltage for 2 h. The voltages chosen for each cell were based on the corresponding potentials of the current peaks, which were observed in the LSV results of each system in Fig. 2a. After that, XPS was performed on the harvested Si anodes.

For post-mortem analysis, cells were dismantled in an argon-filled glovebox after the test. The electrodes were harvested and swirled twice (for 1 min each) in excess dimethyl carbonate (DMC) to remove electrolyte residue such as LiPF₆. However, for half-cell tests, the harvested electrodes were not washed, because washing could lead to delamination of the Si electrode.

XPS. XPS data were acquired using a PHI 5000 VersaProbe II system (Physical Electronics) attached to an argon-atmosphere glovebox. The base pressure was $\sim 1 \times 10^{-8}$ torr. The samples were placed in the XPS chamber by moving them through the glovebox (with no air exposure). The spectra were obtained under the following conditions: 100- μm beam (25 W) with Al K α radiation ($h\nu = 1486.6$ eV), Ar⁺-ion and electron beam sample neutralization, fixed analyzer transmission mode, and pass energy of 23.50 eV. All data were calibrated to the C-C binding energy at 284.80 eV. The estimated uncertainty in the atomic concentrations is 10%.

HPLC/ESI-MS. Five coin cells from each cell system were used to make samples for HPLC/ESI-MS characterization. The entire cell stacks (electrodes, spacers, spring, separator) were combined in a vial containing 3 mL of pristine DMC solvent and soaked for 3–4 hr. The solvent in the vial was then transferred to another vial containing 5 mL of dichloromethane. We took the vial out of the Ar-filled glovebox and added 7 mL HPLC-grade water and 0.1 g Na₂CO₃. The resulting mixture was thoroughly blended using a vortex mixer. The mixture was allowed to stand for 4 h to separate into organic and aqueous layers. The organic layer was expected to contain only the electrolyte decomposition products. It was also expected that the LiPF₆ salt would be in the aqueous layer; the Na₂CO₃ was present to neutralize any nascent HF. Then we pipetted the bottom organic layer out into a clean vial, and left each vial open overnight to evaporate the solvents (DMC and dichloromethane). We then added 0.2 mL of acetonitrile (VWR) and 0.4 mL of HPLC-grade water to each vial and left it for at least 2 h to dissolve the soluble components of the residue. Finally, the sample was characterized using HPLC/ESI-MS (Agilent Technologies 1260 Infinity liquid chromatograph equipped with an Agilent 6120 Quadrupole ESI mass spectrometer detector). For each sample, a 200- μL injection was made via the autosampler. The sample was pumped through a ZORBAX® ODS column (5 μm ; 4.6 \times 250 mm) at 25°C at a flow rate of 1 mL/min. The mobile phase consisted of 60% water and 40% acetonitrile, each containing 0.1 vol % formic acid (HPLC grade, Sigma-Aldrich). The detector capillary voltage was set at 3000 V; the drying-gas (N₂) flow rate was 12 L/min; the nebulizer pressure was 35 psig; the drying gas temperature was 350°C; and the fragmenter voltage was set at 70 V. The detection was done in the positive-ion mode, and the data were collected in the “full” mode.

Data reduction. The data from the galvanostatic cell tests other than the three-electrode tests were taken directly from the cell cycler, and those from the three-electrode tests and LSV tests were taken directly from the vendor-provided CorrWare® software conversion of the data. Data plotting was performed using Origin®.

For the XPS analysis, the Shirley background data were subtracted from all spectra. The spectra were fitted to multiple gaussian peaks by using CasaXPS®, and the fitted data were extracted and plotted using Origin®. Relative atomic concentrations were calculated from the gaussian fits.

The HPLC-TIC data were used to calculate SICs. The relative amount of a given species in a sample was calculated by integrating the peaks in the chromatograms.

Correlations between the atomic concentrations on the negative electrode surface and the relative amounts of species observed in the HPLC were calculated using the CORREL function in Microsoft® Excel®. The value of the correlation coefficient could vary between -1 and 1, corresponding to inverse and direct correlations, respectively. If the absolute value of the correlation coefficient was 0.95 or greater, it indicated a strong relationship between the sets of data. All pairs of data sets with a strong relationship were plotted, such as those shown in Figs. 9a and 9b. The data in Fig. 9a were widely spaced and, thus, the correlation was not biased and was included for further consideration. In Fig. 9b, on the other hand, two points were clustered, skewing the relationship. In effect, the correlation was based on only two points. These data were not used further.

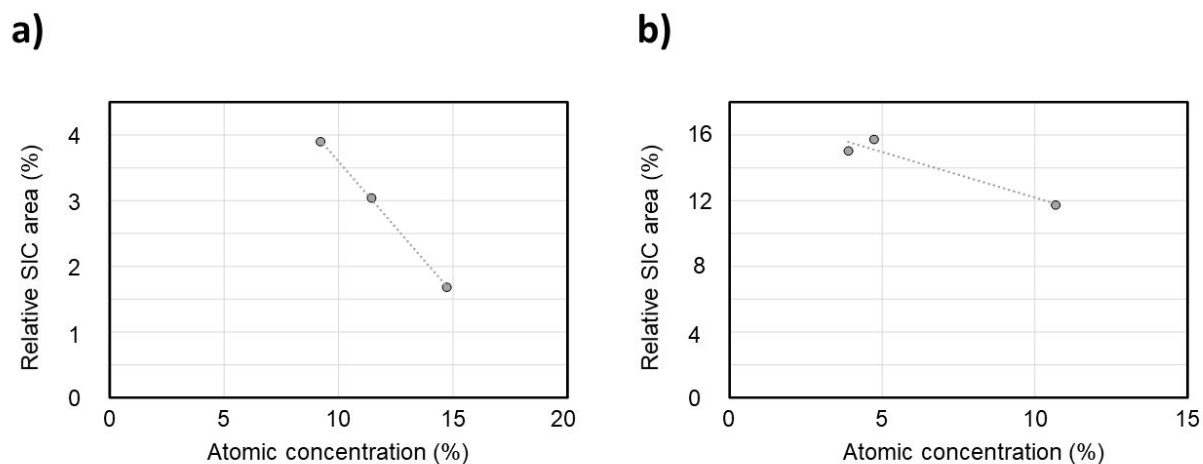


Figure 9. a) Plot of relative SIC area vs. concentration from the XPS, indicating what was considered a valid relationship. The data were widely spaced. b) Plot of relative SIC area vs. concentration from the XPS, indicating what was considered not a valid relationship. The data were not widely spaced.

Conflicts of interests

There are no conflicts to declare.

Acknowledgments

We gratefully acknowledge support from the U. S. Department of Energy (DOE), Vehicle Technologies Office, specifically from Brian Cunningham and David Howell. Argonne National Laboratory is operated for DOE Office of Science by UChicago Argonne, LLC, under contract

number DE-AC02-06CH11357. The views expressed in the article do not necessarily represent the views of the DOE or the U.S. Government. The electrodes used in this article were made by Argonne's Cell Analysis, Modeling and Prototyping (CAMP) Facility, which was supported by the Applied Battery Research for Transportation Program.

The U.S. government retains for itself, and others acting on its behalf, a paid-up nonexclusive, irrevocable worldwide license in said article to reproduce, prepare derivative works, distribute copies to the public, and perform publicly and display publicly, by or on behalf of the government.

REFERENCES

1. Tarascon, J. M.; Armand, M., Issues and challenges facing rechargeable lithium batteries. *Nature* **2001**, *414* (6861), 359-367.
2. Aricò, A. S.; Bruce, P.; Scrosati, B.; Tarascon, J.-M.; van Schalkwijk, W., Nanostructured materials for advanced energy conversion and storage devices. *Nature Materials* **2005**, *4* (5), 366-377.
3. Obrovac, M. N.; Krause, L. J., Reversible Cycling of Crystalline Silicon Powder. *Journal of The Electrochemical Society* **2007**, *154* (2), A103.
4. Obrovac, M. N., Si-alloy negative electrodes for Li-ion batteries. *Current Opinion in Electrochemistry* **2018**, *9*, 8-17.
5. Obrovac, M. N.; Chevrier, V. L., Alloy Negative Electrodes for Li-Ion Batteries. *Chemical Reviews* **2014**, *114* (23), 11444-11502.
6. Lee, S. W.; McDowell, M. T.; Berla, L. A.; Nix, W. D.; Cui, Y., Fracture of crystalline silicon nanopillars during electrochemical lithium insertion. *Proceedings of the National Academy of Sciences* **2012**, *109* (11), 4080.
7. Michalak, B.; Berkes, B. B.; Sommer, H.; Brezesinski, T.; Janek, J., Electrochemical Cross-Talk Leading to Gas Evolution and Capacity Fade in LiNi_{0.5}Mn_{1.5}O₄/Graphite Full-Cells. *The Journal of Physical Chemistry C* **2017**, *121* (1), 211-216.
8. Joshi, T.; Eom, K.; Yushin, G.; Fuller, T. F., Effects of Dissolved Transition Metals on the Electrochemical Performance and SEI Growth in Lithium-Ion Batteries. *Journal of The Electrochemical Society* **2014**, *161* (12), A1915-A1921.
9. Tornheim, A.; Sahore, R.; He, M.; Croy, J. R.; Zhang, Z., Preformed Anodes for High-Voltage Lithium-Ion Battery Performance: Fluorinated Electrolytes, Crosstalk, and the Origins of Impedance Rise. *Journal of The Electrochemical Society* **2018**, *165* (14), A3360-A3368.
10. Komaba, S.; Kumagai, N.; Kataoka, Y., Influence of manganese(II), cobalt(II), and nickel(II) additives in electrolyte on performance of graphite anode for lithium-ion batteries. *Electrochimica Acta* **2002**, *47* (8), 1229-1239.
11. Chen, H.; Ma, T.; Zeng, Y.; Liu, L.; Qiu, X., Study on solid electrolyte interphase excessive growth caused by Mn (II) deposition on silicon anode. *Electrochimica Acta* **2018**, *282*, 602-608.
12. Zheng, H.; Sun, Q.; Liu, G.; Song, X.; Battaglia, V. S., Correlation between dissolution behavior and electrochemical cycling performance for LiNi_{1/3}Co_{1/3}Mn_{1/3}O₂-based cells. *Journal of Power Sources* **2012**, *207*, 134-140.

13. Visser, D. R.; Chen, Z.; Shao, Y.; Engelhard, M.; Das, U.; Redfern, P.; Curtiss, L. A.; Pan, B.; Liu, J.; Amine, K., Role of Manganese Deposition on Graphite in the Capacity Fading of Lithium Ion Batteries. *ACS Applied Materials & Interfaces* **2016**, *8* (22), 14244-14251.
14. Zhan, C.; Lu, J.; Jeremy Kropf, A.; Wu, T.; Jansen, A. N.; Sun, Y.-K.; Qiu, X.; Amine, K., Mn(II) deposition on anodes and its effects on capacity fade in spinel lithium manganate-carbon systems. *Nature Communications* **2013**, *4* (1), 2437.
15. Gallus, D. R.; Schmitz, R.; Wagner, R.; Hoffmann, B.; Nowak, S.; Cekic-Laskovic, I.; Schmitz, R. W.; Winter, M., The influence of different conducting salts on the metal dissolution and capacity fading of NCM cathode material. *Electrochimica Acta* **2014**, *134*, 393-398.
16. Gilbert, J. A.; Shkrob, I. A.; Abraham, D. P., Transition Metal Dissolution, Ion Migration, Electrocatalytic Reduction and Capacity Loss in Lithium-Ion Full Cells. *Journal of The Electrochemical Society* **2017**, *164* (2), A389-A399.
17. Morin, H. R.; Graczyk, D. G.; Tsai, Y.; Lopykynski, S.; Iddir, H.; Garcia, J. C.; Dietz Rago, N.; Trask, S.; Flores, L.; Son, S.-B.; Zhang, Z.; Johnson, N. M.; Bloom, I., Transition-Metal Dissolution from NMC-Family Oxides: A Case Study. *ACS Applied Energy Materials* **2020**, *3* (3), 2565-2575.
18. Sahore, R.; Dogan, F.; Bloom, I. D., Identification of Electrolyte-Soluble Organic Cross-Talk Species in a Lithium-Ion Battery via a Two-Compartment Cell. *Chemistry of Materials* **2019**, *31* (8), 2884-2891.
19. Son, S.-B.; Robertson, D.; Tsai, Y.; Trask, S.; Dunlop, A.; Bloom, I., Systematic Study of the Cathode Compositional Dependency of Cross-Talk Behavior in Li-Ion Battery. *Journal of The Electrochemical Society* **2020**, *167* (16), 160508.
20. Lux, S. F.; Lucas, I. T.; Pollak, E.; Passerini, S.; Winter, M.; Kostecki, R., The mechanism of HF formation in LiPF₆ based organic carbonate electrolytes. *Electrochemistry Communications* **2012**, *14* (1), 47-50.
21. Li, Q.; Liu, X.; Han, X.; Xiang, Y.; Zhong, G.; Wang, J.; Zheng, B.; Zhou, J.; Yang, Y., Identification of the Solid Electrolyte Interface on the Si/C Composite Anode with FEC as the Additive. *ACS Applied Materials & Interfaces* **2019**, *11* (15), 14066-14075.
22. Schroder, K.; Alvarado, J.; Yersak, T. A.; Li, J.; Dudney, N.; Webb, L. J.; Meng, Y. S.; Stevenson, K. J., The Effect of Fluoroethylene Carbonate as an Additive on the Solid Electrolyte Interphase on Silicon Lithium-Ion Electrodes. *Chemistry of Materials* **2015**, *27* (16), 5531-5542.
23. Piernas-Muñoz, M. J.; Yang, Z.; Kim, M.; Trask, S. E.; Dunlop, A. R.; Bloom, I., Effect of temperature on capacity fade in silicon-rich anodes. *Journal of Power Sources* **2021**, *487*, 229322.
24. Kim, M.; Yang, Z.; Bloom, I., Review—The Lithiation/Delithiation Behavior of Si-Based Electrodes: A Connection between Electrochemistry and Mechanics. *Journal of The Electrochemical Society* **2021**, *168* (1), 010523.
25. Liu, S.; Wang, L.; Zhang, C.; Chu, B.; Wang, C.; Huang, T.; Yu, A., Dynamic evolution of Cathode-Electrolyte interface of LiNi_{0.6}Co_{0.2}Mn_{0.2}O₂ during the initial Charge-Discharge process. *Journal of Power Sources* **2019**, *438*, 226979.
26. Wang, H.; Li, X.; Li, F.; Liu, X.; Yang, S.; Ma, J., Formation and modification of cathode electrolyte interphase: A mini review. *Electrochemistry Communications* **2021**, *122*, 106870.
27. Cabana, J.; Kwon, B. J.; Hu, L., Mechanisms of Degradation and Strategies for the Stabilization of Cathode-Electrolyte Interfaces in Li-Ion Batteries. *Accounts of Chemical Research* **2018**, *51* (2), 299-308.
28. Liu, Y.-M.; G. Nicolau, B.; Esbenschade, J. L.; Gewirth, A. A., Characterization of the Cathode Electrolyte Interface in Lithium Ion Batteries by Desorption Electrospray Ionization Mass Spectrometry. *Analytical Chemistry* **2016**, *88* (14), 7171-7177.
29. Takahashi, I.; Kiuchi, H.; Ohma, A.; Fukunaga, T.; Matsubara, E., Cathode Electrolyte Interphase Formation and Electrolyte Oxidation Mechanism for Ni-Rich Cathode Materials. *The Journal of Physical Chemistry C* **2020**, *124* (17), 9243-9248.

30. Lu, W.; Zhang, J.; Xu, J.; Wu, X.; Chen, L., In Situ Visualized Cathode Electrolyte Interphase on LiCoO₂ in High Voltage Cycling. *ACS Applied Materials & Interfaces* **2017**, *9* (22), 19313-19318.
31. Xu, S.; Luo, G.; Jacobs, R.; Fang, S.; Mahanthappa, M. K.; Hamers, R. J.; Morgan, D., Ab Initio Modeling of Electrolyte Molecule Ethylene Carbonate Decomposition Reaction on Li(Ni,Mn,Co)O₂ Cathode Surface. *ACS Applied Materials & Interfaces* **2017**, *9* (24), 20545-20553.
32. Leanza, D.; Mirolo, M.; Vaz, C. A. F.; Novák, P.; El Kazzi, M., Surface Degradation and Chemical Electrolyte Oxidation Induced by the Oxygen Released from Layered Oxide Cathodes in Li-Ion Batteries. *Batteries & Supercaps* **2019**, *2* (5), 482-492.
33. Yu, X.; Manthiram, A., Electrode-electrolyte interfaces in lithium-based batteries. *Energy & Environmental Science* **2018**, *11* (3), 527-543.
34. Choi, N.-S.; Yew, K. H.; Lee, K. Y.; Sung, M.; Kim, H.; Kim, S.-S., Effect of fluoroethylene carbonate additive on interfacial properties of silicon thin-film electrode. *Journal of Power Sources* **2006**, *161* (2), 1254-1259.
35. Ma, D.; Cao, Z.; Hu, A., Si-Based Anode Materials for Li-Ion Batteries: A Mini Review. *Nano-Micro Letters* **2014**, *6* (4), 347-358.
36. McDowell, M. T.; Lee, S. W.; Nix, W. D.; Cui, Y., 25th Anniversary Article: Understanding the Lithiation of Silicon and Other Alloying Anodes for Lithium-Ion Batteries. *Advanced Materials* **2013**, *25* (36), 4966-4985.
37. Iaboni, D. S. M.; Obrovac, M. N., Li₁₅Si₄ Formation in Silicon Thin Film Negative Electrodes. *Journal of The Electrochemical Society* **2016**, *163* (2), A255-A261.
38. Aurbach, D.; Markovsky, B.; Rodkin, A.; Cojocaru, M.; Levi, E.; Kim, H.-J., An analysis of rechargeable lithium-ion batteries after prolonged cycling. *Electrochimica Acta* **2002**, *47* (12), 1899-1911.
39. Sasaki, T.; Abe, T.; Iriyama, Y.; Inaba, M.; Ogumi, Z., Formation mechanism of alkyl dicarbonates in Li-ion cells. *Journal of Power Sources* **2005**, *150*, 208-215.
40. Gachot, G.; Grugeon, S.; Armand, M.; Pilard, S.; Guenot, P.; Tarascon, J.-M.; Laruelle, S., Deciphering the multi-step degradation mechanisms of carbonate-based electrolyte in Li batteries. *Journal of Power Sources* **2008**, *178* (1), 409-421.
41. Schultz, C.; Kraft, V.; Pyschik, M.; Weber, S.; Schappacher, F.; Winter, M.; Nowak, S., Separation and Quantification of Organic Electrolyte Components in Lithium-Ion Batteries via a Developed HPLC Method. *Journal of The Electrochemical Society* **2015**, *162* (4), A629-A634.
42. Gireaud, L.; Grugeon, S.; Pilard, S.; Guenot, P.; Tarascon, J.-M.; Laruelle, S., Mass Spectrometry Investigations on Electrolyte Degradation Products for the Development of Nanocomposite Electrodes in Lithium Ion Batteries. *Analytical Chemistry* **2006**, *78* (11), 3688-3698.
43. Liu, Y.-H.; Takeda, S.; Kaneko, I.; Yoshitake, H.; Yanagida, M.; Saito, Y.; Sakai, T., An approach of evaluating the effect of vinylene carbonate additive on graphite anode for lithium ion battery at elevated temperature. *Electrochemistry Communications* **2015**, *61*, 70-73.